International Journal of Mathematics, Statistics, and Computer Science
Vol. 4
eISSN 2704-1069, DOI: https://doi.org/10.59543/559x5x12

Hemodynamic Simulation of Fusiform Aneurysms under Pulsatile Flow with Shear-Dependent Blood Rheology

Farjana Mitu [1, a)], Chinmayee Podder [1,*, b)] and Ashish Kumar Saha [2, c)]

[1)]Department of Mathematics, University of Barishal, Kornokathi, Barishal-8254, Bangladesh
[2)] Sher-e-Bangla Medical College Hospital, Barishal-8200, Bangladesh

[a)] farjanamitu055@gmail.com [b)] cpodder@bu.ac.bd ; [c)] drashishmmc@gmail.com

Received 07.03.2026, Revised 25.04.2026, Accepted 30.05.2026

ABSTRACT: Bio-mechanical and hemodynamical changes happen due to fusiform aneurysms which alter flow structure and shear stress distribution along the affected segment. This study applies three-dimensional CFD analysis to investigate the hemodynamic environment associated with fusiform aneurysms under physiologically realistic pulsatile blood flow. Numerical simulations are performed in COMSOL Multiphysics using finite element methods, incorporating both Newtonian and Carreau non-Newtonian rheology to evaluate the influence of blood viscosity behavior. Key hemodynamic quantities velocity fields, pressure distribution, WSS, OSI, TAWSS, and RRT are quantified to characterize the flow response to the elongated aneurysmal deformation. Peak systolic velocity is 0.87% lower in the Carreau model compared to the Newtonian model, while diastolic velocity decreases by 11.6%. Peak WSS at systole differs by approximately 9.75% between models, whereas the minimum TAWSS in the aneurysm sac is up to 9% lower under Carreau rheology. The maximum OSI in the sac increases by 0.87% for the non-Newtonian case, indicating greater flow reversal sensitivity, and the maximum RRT increases by roughly 2.6%, suggesting enlarged thrombus-prone zones. These findings demonstrate that the choice of rheological model significantly influences diastolic-phase hemodynamics and thrombus risk indicators, underscoring the importance of non-Newtonian modeling for accurate fusiform aneurysm assessment.

Keywords: Fusiform aneurysm, CFD, Pulsatile blood flow, Carreau model, WSS, OSI, TAWSS, RRT.

1. INTRODUCTION

Fusiform aneurysms are characterized by a gradual, longitudinal expansion of the arterial lumen, which fundamentally alters flow structure and shear stress distribution along the affected segment. Computational studies have demonstrated that non-Newtonian blood models play a critical role in capturing these hemodynamic features. The Carreau and Carreau–Yasuda formulations consistently predict lower wall shear stress and higher relative residence time within fusiform aneurysms than Newtonian assumptions, especially during diastolic or low-shear phases [3,7,13]. Pulsatile simulations further reveal the presence of persistent vortical structures and elevated oscillatory shear index within the aneurysmal core, indicating a disturbed flow environment associated with endothelial dysfunction and thrombus susceptibility [5,10,11,14]. Additionally, variations in aneurysm length, diameter, and vessel curvature have been shown to influence the extent and intensity of low-shear and recirculation zones [1,2,9]. Overall, these findings emphasize that incorporating shear-thinning rheology together with time-dependent inflow conditions is essential for obtaining physiologically meaningful predictions of flow disturbance, wall stress distribution, and aneurysm-related risk in fusiform geometries [4,8,12]. This study provides a unified evaluation of WSS, OSI, TAWSS, and RRT under pulsatile non-Newtonian flow in a fusiform aneurysm, enabling a more complete hemodynamic characterization than studies that examine only one or two indicators. A systematic quantitative comparison between Newtonian and Carreau rheology is performed across spatial locations and cardiac cycle phases, including percentage differences, to capture viscosity dependent variations in flow behavior within the aneurysmal geometry. The analysis further demonstrates that the choice of viscosity model significantly affects the predicted extent and intensity of thrombus prone regions.

2. COMPUTATIONAL METHODOLOGY

2.1 Geometric Modeling

An extended arterial model with a fusiform aneurysm is generated in SolidWorks, capturing a smooth and symmetric longitudinal dilation of the vessel. The artery is defined with a total length of 200 mm

and a baseline lumen diameter of 20 mm, while the aneurysmal region spans 65 mm and attains a maximum diameter of 55 mm, consistent with the dimensions reported by Lim, Jiaqi et al. [11].

FIGURE 1. 3D geometry of fusiform aneurysm

2.2 Governing Equations and Rheological Models:

2.2.1 Continuity Equation

Blood flow within the arterial domain is modeled based on the fundamental principle of conservation of mass. Assuming three dimensional, incompressible, and steady flow, the continuity equation is given by [19,20]

$$\nabla . \boldsymbol{u} = 0 \tag{1}$$

where $\boldsymbol{u} = (u_x, u_y, u_z)$ denotes the velocity vector field.

2.2.2 Momentum Equation (Navier–Stokes)

The motion of blood is governed by the conservation of linear momentum, described by the Navier–Stokes equations for incompressible flow. In vector form, the governing equation is [19,20]:

$$\rho\left(\frac{\partial \boldsymbol{u}}{\partial t} + \boldsymbol{u}.\nabla \boldsymbol{u}\right) = -\nabla p + \nabla . \boldsymbol{\tau} + \boldsymbol{f} \tag{2}$$

where ρ denotes the fluid density, $\boldsymbol{u}$ the velocity vector, p the pressure field, $\boldsymbol{\tau}$ the viscous stress tensor, and $\boldsymbol{f}$ the body force per unit volume. In arterial blood flow, body forces are considered negligible compared to pressure and viscous effects.

The viscous stress tensor is defined as [19]:

$$\boldsymbol{\tau} = 2\mu(\dot{\gamma})\boldsymbol{D} \tag{3}$$

where $\mu(\dot{\gamma})$ denotes the dynamic viscosity, which may be constant or shear-rate dependent, and $\boldsymbol{D}$ is the rate of deformation tensor.

The rate of deformation tensor is given by [19]:

$$\boldsymbol{D} = \frac{1}{2}(\nabla \boldsymbol{u} + (\nabla \boldsymbol{u})^T) \tag{4}$$

where $(\nabla \boldsymbol{u})^T$ represents the transpose of the velocity gradient tensor.

2.2.3 Constitutive Models

Although blood is a complex multiphase suspension composed of plasma and cellular components, it is commonly idealized as either a Newtonian or a non-Newtonian fluid for computational modeling. The Navier–Stokes equations remain identical for both models. The distinction arises solely from the constitutive relation defining the viscous stress tensor.

Newtonian Fluid Model

In the Newtonian assumption, blood is treated as a homogeneous incompressible fluid with constant dynamic viscosity. The constitutive relation is given by [19,20]:

$$\boldsymbol{\tau} = 2\mu \boldsymbol{D} \tag{5}$$

where μ is the dynamic viscosity. In this case, viscosity is independent of shear rate, making the model suitable for simplified arterial flow analysis.

Carreau Non-Newtonian Model

To account for the shear-thinning behavior observed under physiological conditions, a non-Newtonian formulation is often adopted. In this formulation, viscosity varies with shear rate as [20]:

$$\mu(\dot{\gamma}) = \mu_\infty + (\mu_0 - \mu_\infty)[1 + (\lambda\dot{\gamma})^2]^{\frac{n-1}{2}} \tag{6}$$

and the stress tensor is expressed as [19]:

$$\boldsymbol{\tau} = 2\mu(\dot{\gamma})\boldsymbol{D} \tag{7}$$

where μ_0 and μ_∞ represent the viscosities at zero and infinite shear rates, respectively, λ is a characteristic time constant, and n is the flow behavior index. This formulation enables a more realistic representation of blood rheology across a wide range of shear conditions, particularly in regions of disturbed or low-shear flow.

2.3 Boundary Conditions:

The blood flow is modeled as incompressible with a density of 1060 kg/m^3 [16]. Two rheological descriptions are employed: a Newtonian model with constant viscosity $\mu = 0.00345\ Pa \cdot s$ [17], and a non-Newtonian Carreau formulation characterized by $\mu_\infty = 0.00345\ Pa \cdot s$, $\mu_0 = 0.056\ Pa \cdot s$, $\lambda = 3.313$, and n = 0.3568 [18]. Pulsatility is introduced at the inlet through a time-dependent velocity function,

$$u(t) = 1 + \sin\left(2\pi\frac{t}{T}\right) \tag{1}$$

representing a single cardiac cycle [15]. Rigid arterial walls with no-slip boundary conditions are assumed, and 0 Pa pressure condition is prescribed at the outlet [15].

2.4 Mesh and Time Stepping:

A mesh refinement and time discretization strategy is adopted to ensure numerical accuracy and mesh-independent solutions. All simulations are performed using a uniform time step of 0.01 s, which provides adequate temporal resolution for pulsatile flow while maintaining numerical stability. Mesh independence is achieved for the Newtonian model with a finer mesh of 633,952 elements and for the Carreau model with a fine mesh of 5,866 elements, ensuring accurate hemodynamic resolution and computational efficiency.

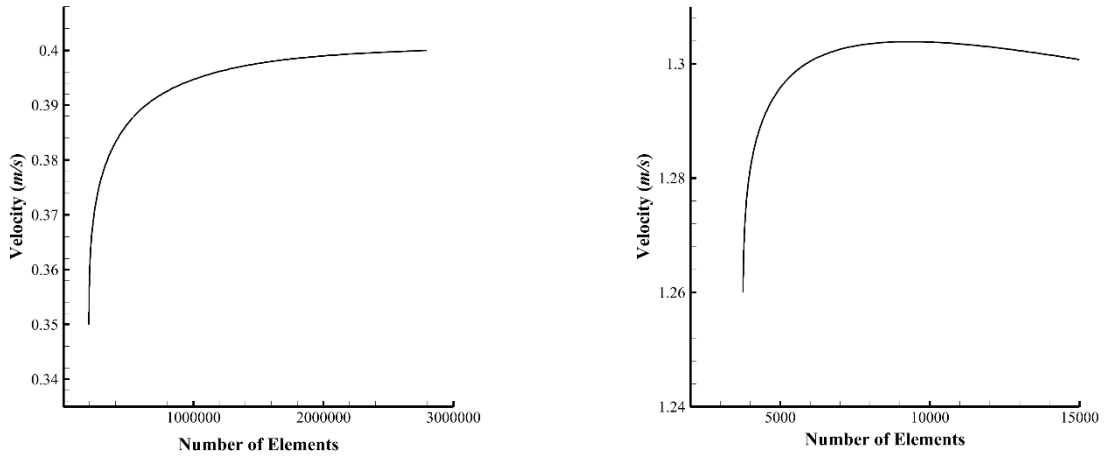

(a) (b)

FIGURE 2. Mesh independence for aneurysmal artery geometry using (a) Newtonian model and (b)Carreau model

2.5 Validation:

The numerical framework is validated by comparing the predicted velocity field with the reference results of Siebert et al. [6]. A quantitative comparison is presented in **Table 1**.

Table 1. Quantitative Comparison of Velocity with Reference Data

Parameter	Reference Value (m/s)	Computed Value (m/s)	Relative Error (%)
Velocity	0.025	0.0026	6.4

The observed deviation can be attributed to differences in mesh resolution, solver formulation, and boundary condition implementation. The close agreement in flow patterns and velocity distribution, especially in accelerated and recirculating regions, supports the reliability of the present model as shown in **FIGURE 3**.

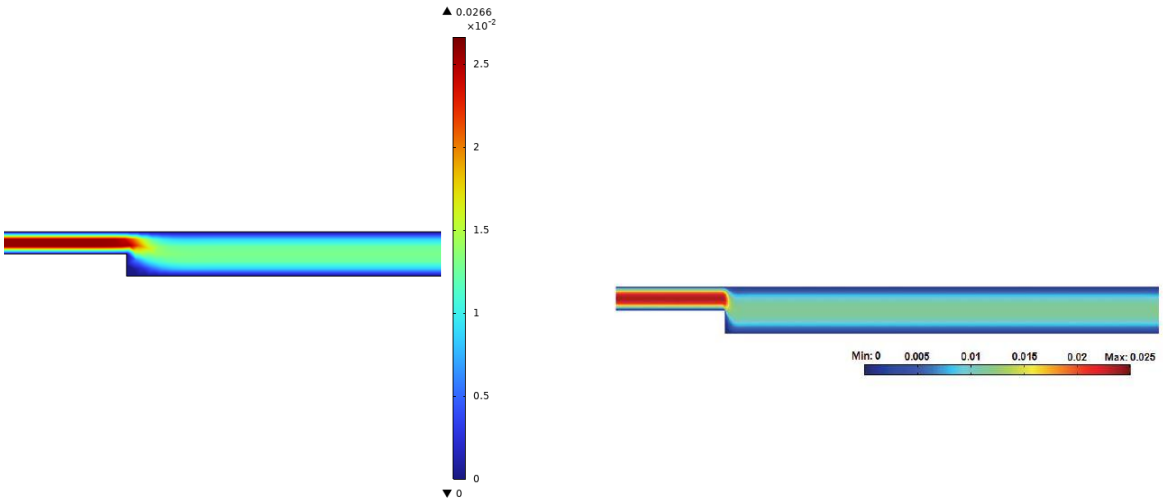

(a) (b)

FIGURE 3. Comparison of velocity field $(m/s)$for (a) the present study and (b) the reference results from Siebert et al.

3. RESULTS AND DISCUSSION

This section presents the numerical results obtained from the simulations and provides a detailed discussion of the underlying hemodynamic behavior. The results are illustrated through figures, tables, and graphical representations to facilitate clear interpretation of flow characteristics. The discussion is organized into relevant subsections, focusing on key hemodynamic parameters and flow characteristics.

3.1. Velocity

At t = 0.25 s (peak systole), a high velocity jet enters the aneurysm sac and impinges on the distal wall, generating symmetric recirculation vortices. The peak velocity is 2.29 m/s for the Newtonian model and 2.27 m/s for the Carreau model, corresponding to a difference of 0.87%. This small deviation is attributed to high shear rates that drive Carreau viscosity toward its infinite shear limit, resulting in near Newtonian behavior. Despite close agreement, the Newtonian model exhibits sharper velocity gradients and larger recirculation zones, whereas the Carreau model produces smoother velocity transitions and more confined vortical structures, reflecting shear thinning effects that moderate flow acceleration and stabilize the central flow.

At t = 0.75 s (diastole), the Newtonian model predicts a higher peak velocity (0.751 m/s) with pronounced recirculation and fragmented vortical structures, indicating increased flow instability. In contrast, the Carreau model yields a lower peak velocity (0.664 m/s) and a more diffused flow field due to increased effective viscosity under low shear conditions. Across the cardiac cycle, velocity peaks at systole and decreases during diastole, with more uniform flow behavior observed in the Carreau model, reflecting its ability to stabilize intra-aneurysmal dynamics and suppress recirculation.

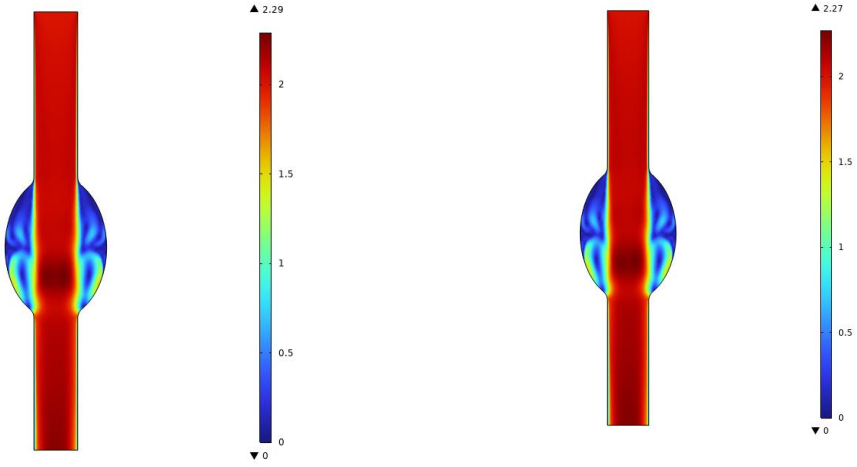

(a) (b)

FIGURE 4. Velocity magnitude contours (m/s) at t = 0.25 s for (a) Newtonian model and (b) Carreau model

(a) (b)

FIGURE 5. Cross-sectional streamlines at t = 0.25 s for (a) Newtonian model and (b)Carreau model

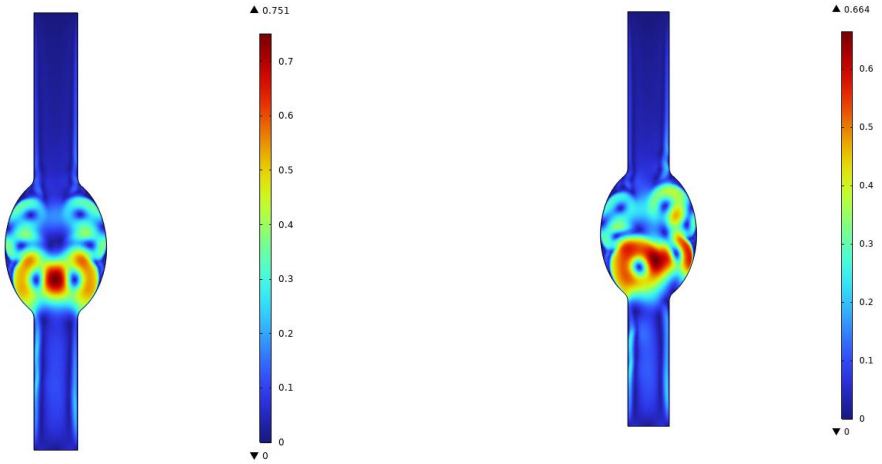

(a) (b)

FIGURE 6. Velocity magnitude contours (m/s) at t = 0.75 s for (a) Newtonian model and (b) Carreau model

(a) (b)

FIGURE 7. Cross-sectional streamlines at t = 0.75 s for (a) Newtonian model and (b)Carreau model

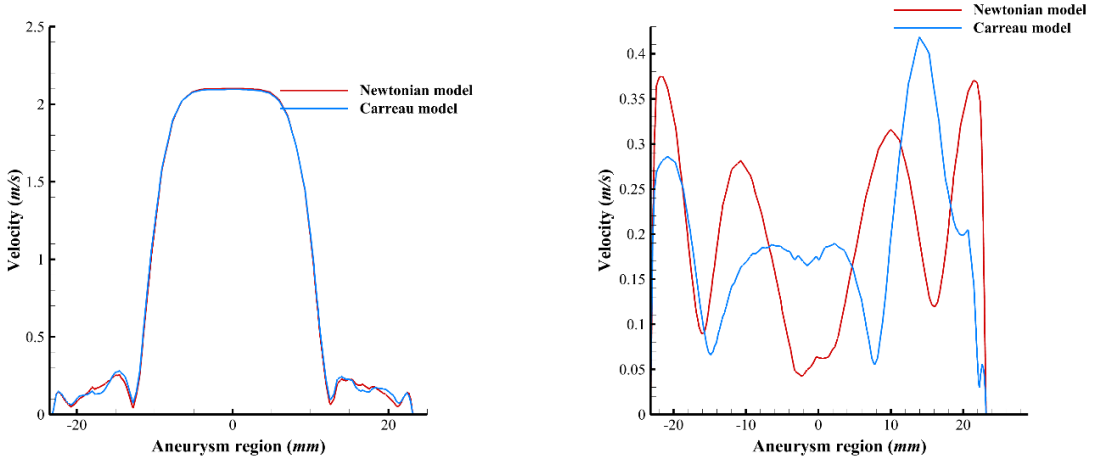

(a) (b)

FIGURE 8. Axial velocity distributions (m/s) within the aneurysmal region for Newtonian and Carreau fluid models at (a) $t = 0.25s$ and (b) $t = 0.75s$

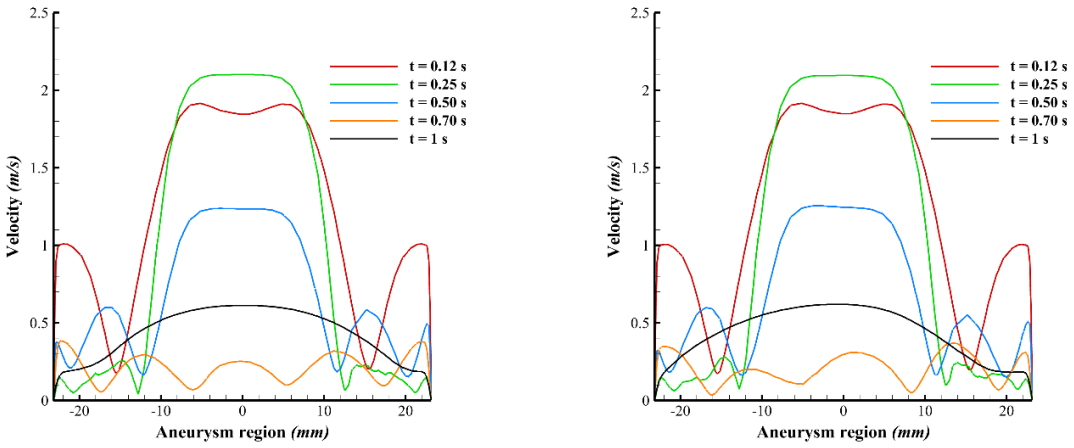

(a) (b)

FIGURE 9. Velocity distribution (m/s) along the aneurysm region for (a) Newtonian and (b) Carreau models

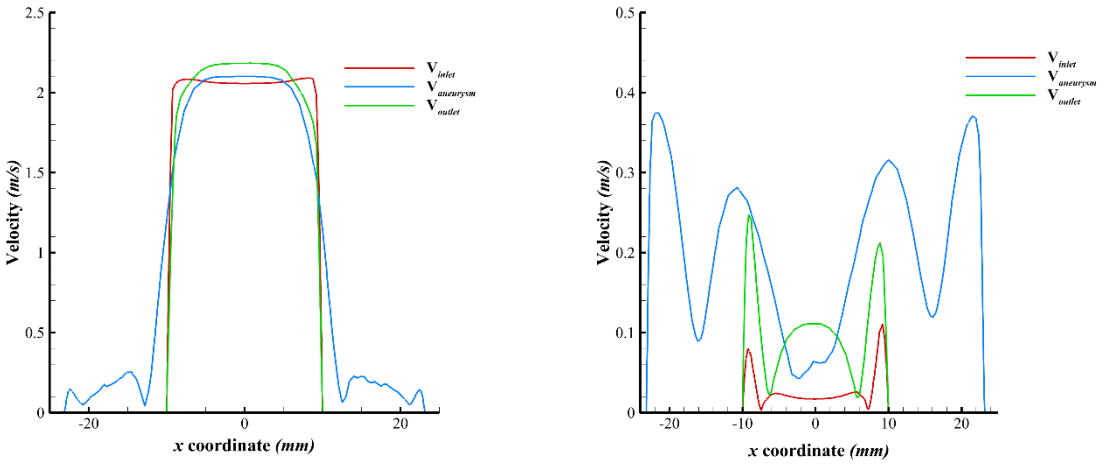

(a) (b)

FIGURE 10. Spatial velocity distribution (m/s) for the Newtonian model at (a) $t = 0.25\ s$ and (b) $t = 0.75\ s$

3.2. Pressure:

The pressure field is governed by the balance between inertial and viscous forces. At peak systole (t = 0.25 s), a high-pressure region develops upstream of the aneurysm, followed by a sharp pressure drop across the inlet neck due to flow acceleration. Within the aneurysm sac, the pressure becomes relatively uniform as a result of geometric expansion and reduced velocity, with localized low-pressure regions associated with flow separation and recirculation. The pressure difference between the two models at systole is small (less than 2%).

At diastole (t = 0.75 s), the pressure field weakens and redistributes, with the Carreau model predicting slightly higher pressure within the sac due to increased viscous resistance under low shear conditions. Compared to the Newtonian model, the Carreau model exhibits smoother pressure gradients, reflecting the damping effect of shear-thinning viscosity on pressure variations.

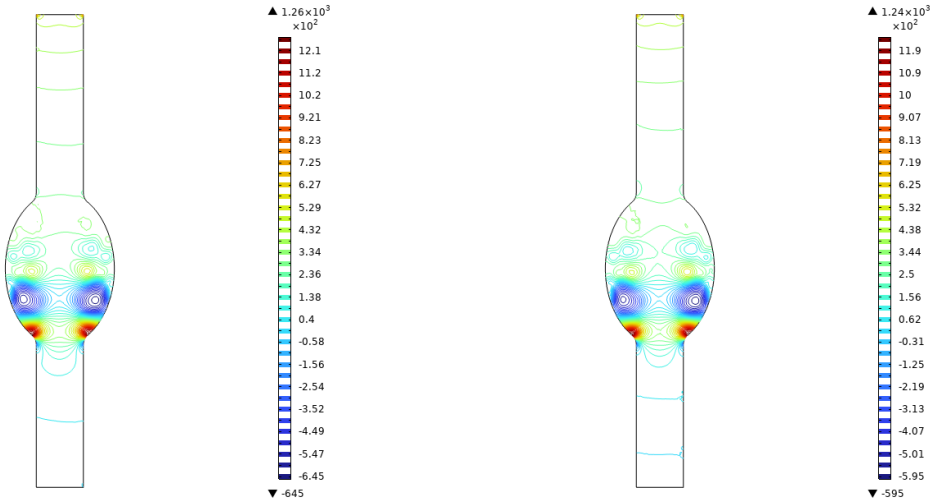

(a) (b)

FIGURE 11. Pressure contours (Pa) at 0.25 s for (a) Newtonian model and (b) Carreau model

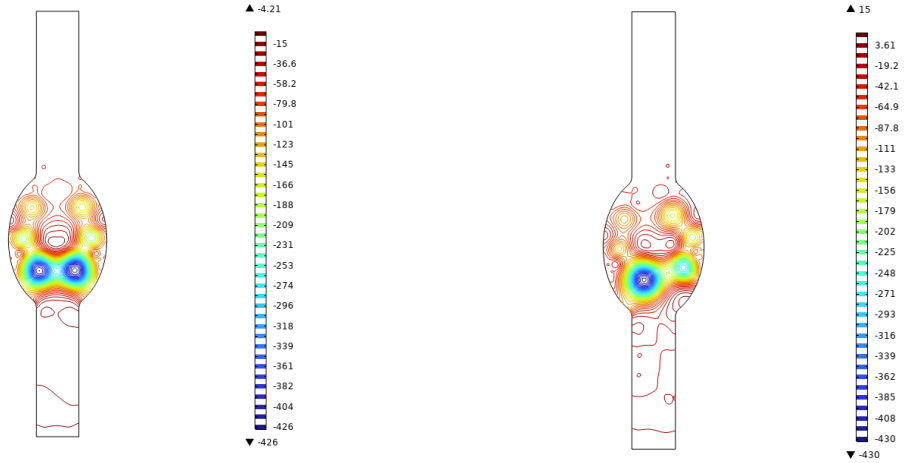

(a) (b)

FIGURE 12. Pressure contours (Pa) at 0.75 s for (a) Newtonian model and (b) Carreau model

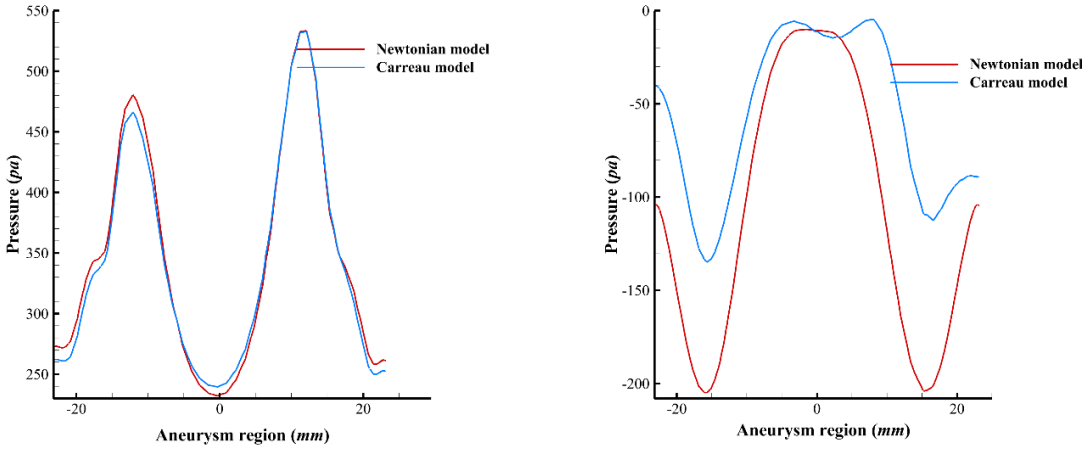

(a) (b)

FIGURE 13. Pressure distributions for Newtonian and Carreau models at (a) $t = 0.25\ s$ and (b) $t = 0.75\ s$

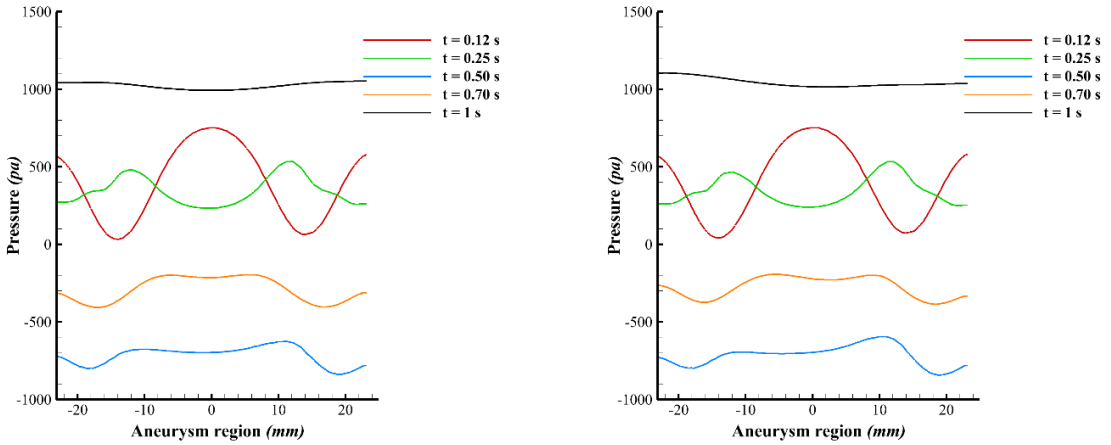

(a) (b)

FIGURE 14. Pressure distributions along the aneurysmal region for (a) the Newtonian model and (b) the Carreau model

3.3 WSS:

WSS is a critical hemodynamic parameter implicated in endothelial mechanotransduction, vascular remodeling, and thrombus formation. The arterial wall shear stress is expressed as

$$\tau_{WSS} = -\mu \left(\frac{\partial v}{\partial r}\right)_{wall} \tag{1}$$

where v denotes the velocity component in the flow direction, r represents the radial direction normal to the arterial wall, μ is the dynamic viscosity of blood, and $\left(\frac{\partial v}{\partial r}\right)_{wall}$ is the velocity gradient evaluated at the wall surface. The negative sign indicates the direction of shear stress acting opposite to the increasing velocity gradient at the boundary.

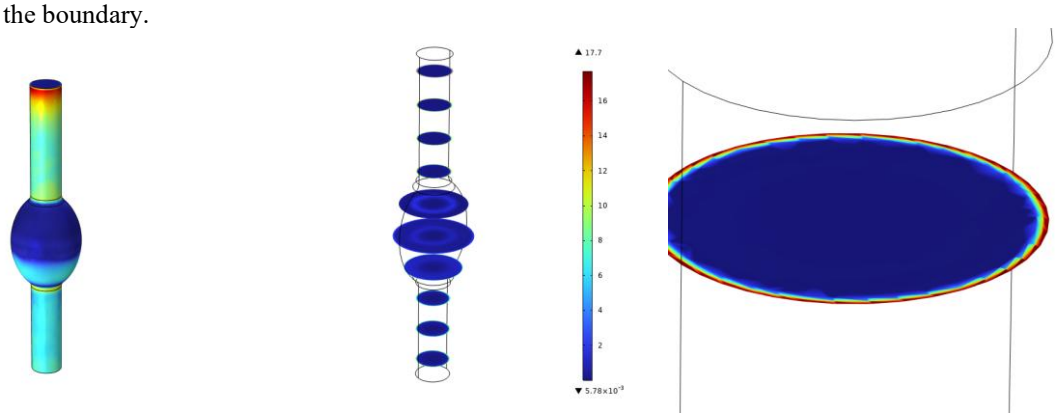

FIGURE 15. 3D surface and slice views of WSS (Pa) at t = 0.25 s for Newtonian model

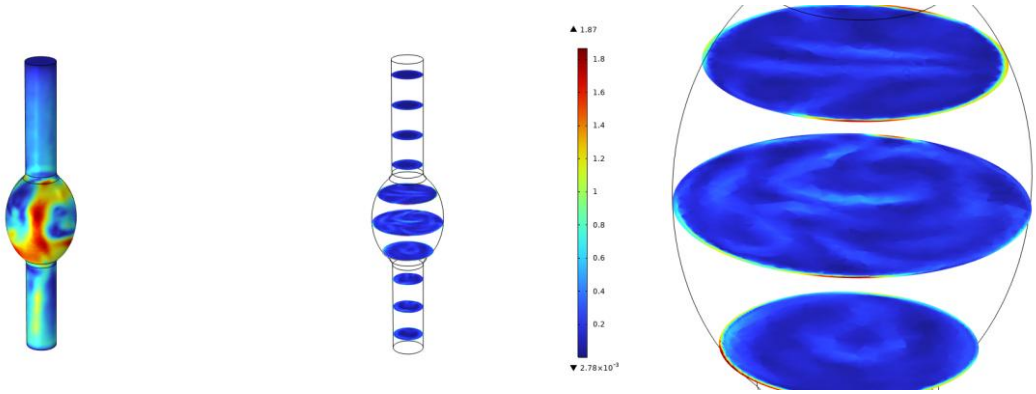

FIGURE 16. 3D surface and slice views of WSS (Pa) at t = 0.75 s for Newtonian model

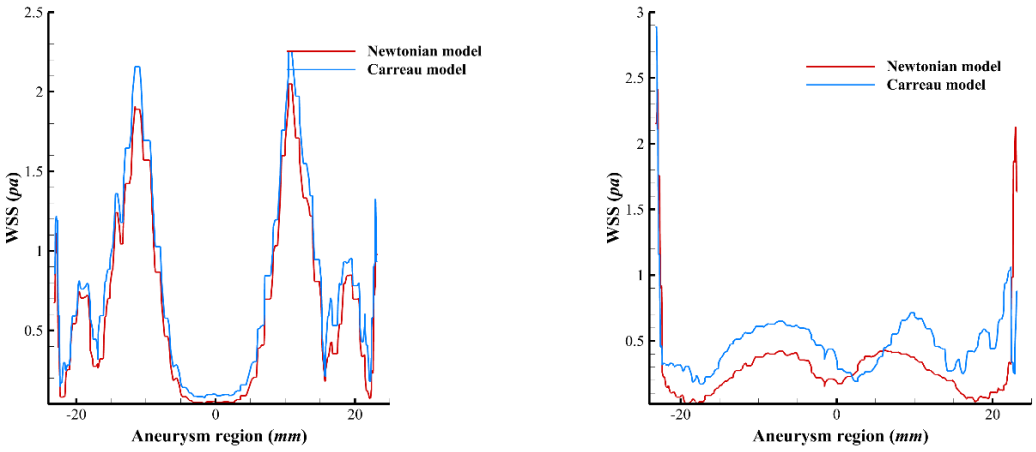

(a) (b)

FIGURE 17. Comparison of WSS distributions at (a) $t = 0.25\ s$ and (b) $t = 0.75\ s$

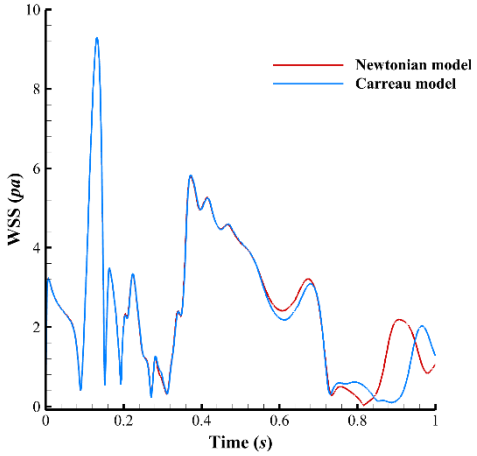

FIGURE 18. WSS profile (Pa) over the cardiac cycle at a selected point on the aneurysmal wall

At peak systole (t = 0.25 s), high WSS values are concentrated at the inlet and outlet necks due to flow acceleration through geometric constrictions, while reduced values are observed within the aneurysm sac as a result of flow deceleration and recirculation. The peak WSS at systole is approximately 10% lower under Carreau rheology compared to the Newtonian case. At diastole (t = 0.75 s), this difference increases to approximately 20% in the sac region. This increased reduction arises from lower shear rates during diastole, where the Carreau model predicts higher effective viscosity, leading to stronger damping of velocity gradients and further reduction in wall shear stress.

3.4 TAWSS:

The time averaged wall shear stress is defined as:

$$\text{TAWSS} = \frac{1}{T}\int_0^T |\tau_{WSS}|\, dt \tag{1}$$

where T represents the cardiac cycle period and τ_{WSS} denotes the instantaneous wall shear stress.

Figure 19 shows that TAWSS is elevated near the inlet due to direct flow impingement and strong velocity gradients. Upon entering the aneurysm sac, TAWSS decreases significantly as a result of geometric expansion, flow deceleration, and recirculation, with minimum values observed near the sac core. The Carreau model predicts approximately 9.8% lower minimum TAWSS in the sac compared to the Newtonian model, whereas differences at the inlet and outlet remain below 3%. This reduction arises from increased effective viscosity under low shear conditions, which further weakens momentum transfer to the wall.

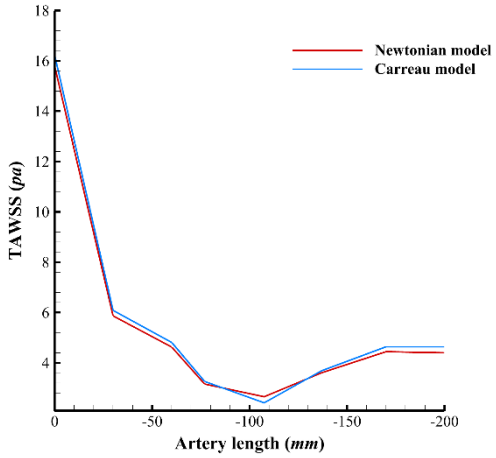

FIGURE 19. Comparison of TAWSS (Pa) along the arterial length for Newtonian and Carreau fluid models

3.5 OSI:

The OSI quantifies the directional variation of wall shear stress over the cardiac cycle:

$$\mathrm{OSI} = \frac{1}{2}\left(1 - \frac{\left|\int_0^T \tau_{WSS} dt\right|}{\int_0^T |\tau_{WSS}|\, dt}\right) \quad (1)$$

where T represents the cardiac cycle period and τ_{WSS} denotes the instantaneous wall shear stress.

OSI ranges from 0 for unidirectional flow to 0.5 for purely oscillatory flow. **FIGURE 20** shows that OSI is minimal at the inlet, reflecting stable flow, and increases downstream due to geometric effects. Elevated OSI is observed within the aneurysm sac as a result of flow separation, recirculation, and vortex formation, which induce frequent shear reversal. The Carreau model predicts approximately 0.87% higher maximum OSI compared to the Newtonian case, indicating enhanced sensitivity to flow reversal under non-Newtonian conditions. This increase arises from elevated local viscosity, which amplifies the contribution of reversed shear to the time integrated wall shear stress.

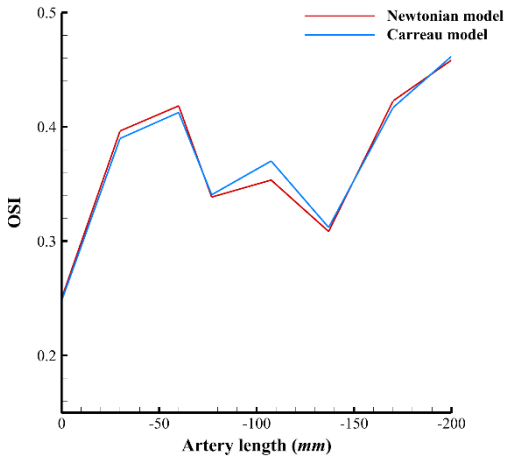

FIGURE 20. Comparison of OSI along the arterial length for Newtonian and Carreau fluid models

3.6 RRT:

Relative residence time combines information from TAWSS and OSI to identify regions where blood particles remain near the wall for extended periods:

$$\mathrm{RRT} = \frac{1}{\mathrm{TAWSS} \cdot (1 - 2 \cdot \mathrm{OSI})} \quad (1)$$

High RRT values indicate prolonged near wall residence, promoting platelet activation and thrombus formation.

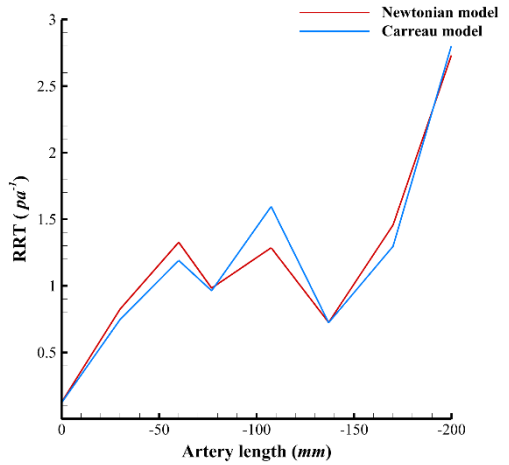

FIGURE 21. Comparison of RRT (Pa^{-1}) along the arterial length for Newtonian and Carreau fluid models

FIGURE 21 shows the RRT distribution. The Carreau model predicts approximately 2.64% higher maximum RRT within the aneurysm sac, indicating that the thrombus prone region is both larger and more intense under non-Newtonian conditions. This is consistent with the combined effect of reduced TAWSS and elevated OSI in the sac, where increased effective viscosity under low shear conditions slows near wall flow and increases residence time.

3.7 Summary of Hemodynamic Metrics

Table 2 summarizes the key hemodynamic quantities predicted by each rheological model. The percentage differences highlight the sensitivity of each metric to the viscosity model.

Table 2. Comparison of hemodynamic metrics between Newtonian and Carreau models

Metric	Newtonian	Carreau	% Diff.	Location
Peak systolic velocity(m/s)	2.29	2.27	0.87	Centerline
Diastolic velocity(m/s)	0.751	0.664	11.6	Centerline
Peak systolic pressure (Pa)	1.26×10^3	1.24×10^3	1.61	Distal aneurysm neck
Peak WSS, systole (Pa)	2.05	2.25	9.75	Inlet neck
Min TAWSS(Pa)	2.651	2.414	9.8	Sac center
Max OSI	0.458	0.462	0.87	Sac center
Max RRT(Pa^{-1})	2.731	2.803	2.64	Sac center

3.8 Dimensionless Flow Characterization and Mechanistic Effects of Carreau Rheology

To characterize the flow regime and provide a physical basis for the modeling framework, relevant dimensionless parameters are considered together with the rheological behavior of blood.
The Reynolds number, defined as

$$Re = \frac{\rho U D}{\mu}$$

represents the ratio of inertial to viscous forces. Due to the pulsatile nature of blood flow, the Reynolds number varies over the cardiac cycle, increasing during systole and decreasing during diastole.
In the Newtonian formulation, constant viscosity yields a uniform Reynolds number for given flow conditions. In contrast, under the Carreau model, viscosity varies with shear rate, leading to spatial and temporal variation of the effective Reynolds number. In low shear regions such as the aneurysm sac, increased viscosity reduces the local Reynolds number, enhancing viscous dominance and flow stabilization. In high shear regions near the inlet and outlet neck, viscosity approaches its lower limit, resulting in behavior similar to the Newtonian case.
Although instantaneous values may indicate transitional tendencies during peak flow, the combined effects of pulsatility and viscous damping maintain predominantly laminar flow. Therefore, a laminar flow framework is adopted.
The Womersley number is given by

$$\alpha = \left(\frac{D}{2}\right)\sqrt{\frac{2\pi f \rho}{\mu}}$$

and represents the relative importance of unsteady inertial effects in pulsatile flow. A value greater than unity indicates strong temporal variation of the velocity profile, deviating from a quasi steady distribution. This confirms the necessity of a transient formulation to capture phase dependent hemodynamic behavior.
These dimensionless parameters provide a global characterization of the flow regime, while the rheological behavior of blood governs local hemodynamic variations.

The differences observed between the Newtonian and Carreau models are explained by the shear dependent viscosity behavior of the Carreau constitutive law. In low-shear regions within the aneurysm sac, where recirculation velocities are small and velocity gradients are weak, the effective viscosity under the Carreau model increases toward the zero-shear limit $\mu_0 = 0.056\ Pa \cdot s$, which is approximately 16 times the

Newtonian reference value of $0.00345\ Pa \cdot s$. This elevated viscosity in the sac dampens velocity gradients, reduces the near-wall shear rate, and consequently lowers the wall shear stress.
As a result, TAWSS decreases and RRT increases within the aneurysm sac [8,17]. Conversely, in high-shear regions at the inlet neck and outlet neck, where the flow accelerates through geometric constrictions, the local shear rate is sufficiently large that the Carreau viscosity approaches $\mu_\infty = 0.00345\ Pa \cdot s$, effectively recovering Newtonian behavior.
This explains the small differences in peak systolic velocity and wall shear stress, while diastolic phase parameters and sac centered indices exhibit significantly larger variations. The increase in OSI under Carreau rheology can be attributed to the enhanced viscous damping during the low-shear phases of the cardiac cycle. As viscosity increases during diastole, the magnitude of the instantaneous WSS vector decreases, but the directional reversal associated with recirculation persists. Because OSI measures the ratio of net shear to total shear magnitude, a reduction in forward shear leads to a higher OSI value. The combined effect of reduced TAWSS and elevated OSI under the Carreau model produces a synergistic increase in RRT, expanding the predicted extent of the thrombus-prone zone [11, 18].

4. LIMITATION

Despite providing detailed hemodynamic insights, the present study has several limitations. The aneurysm geometry is idealized as a smooth, axisymmetric dilation, which does not capture patient-specific irregularities such as asymmetry or wall thickness variation. The arterial wall is assumed rigid, neglecting deformation and fluid–structure interaction effects that may influence local shear stress. Boundary conditions are not patient-specific, as a generic inlet waveform and zero-gauge outlet pressure are employed without accounting for downstream vascular impedance. Additionally, turbulence modeling is not included; although the peak Reynolds number suggests possible transitional behavior, such effects are not captured in the present framework. Future work should incorporate patient-specific data, compliant walls, and advanced turbulence modeling to improve physiological accuracy.

5. CONCLUSION

Aneurysm geometry and blood rheology exert a critical influence on intra-aneurysmal flow patterns and the distribution of associated hemodynamic risk factors. Peak velocities and pressures typically occur at the aneurysm inlet and neck, where flow acceleration and impingement increase local wall stress, thereby elevating the potential for endothelial injury and progressive aneurysm expansion. Elevated WSS at these regions can stimulate structural remodeling of the arterial wall, while regions of low wall shear stress within the aneurysmal sac, particularly when coupled with high OSI and prolonged RRT, promote flow stagnation, platelet aggregation, and thrombus formation. Vortical structures near lateral walls and distal aneurysm regions further intensify these low-shear environments. The Carreau shear-thinning model moderates extreme velocities and pressures, smooths spatial WSS distributions, and confines vortices closer to the wall, providing a more physiologically realistic and detailed evaluation of areas at risk for thrombosis and aneurysm progression.

NOMENCLATURE

CFD	Computational Fluid Dynamics	RRT	Relative residence time
t	Time	TAWSS	Time Average Wall Shear Stress
T	Time period	WSS	Wall Shear Stress
OSI	Oscillatory shear index		

Funding: This research received no external funding.
Conflict of interest: The authors declare no conflicts of interest..

REFERENCES

[1] Y. A. C. S. &. T. Algabri, "An Investigation of Pulsatile Blood Flow in An Angulated Neck of Abdominal Aortic Aneurysm Using Computational Fluid Dynamics," *Journal of Advanced Research in Fluid Mechanics and Thermal Sciences,* vol. 57, no. 2, pp. 265-274, 2019.

[2] S. W. M. R. W. &. C. X. Baheri Islami, "Virtual reality visualization of CFD simulated blood flow in cerebral aneurysms treated with flow diverter stents," *Applied Sciences,* vol. 11, no. 17, p. 8082, 2021.

[3] D. M. A.-R. M. T. A. a. B. L. Belkacemi, "Flow behaviour and wall shear stress derivatives in abdominal aortic aneurysm models: A detailed CFD analysis into asymmetry effect," *CFD Lett,* vol. 14, pp. 60-74, 2022.

[4] C. &. A. K. Bilgi, "Numerical investigation of the effects of blood rheology and wall elasticity in abdominal aortic aneurysm under pulsatile flow conditions," *Biorheology,* vol. 56, no. 1, pp. 51-71, 2019.

[5] S. T. K. T. H. O. T. K. H. H. A. S. T. U. Y. I. T. O. K. a. K. K. Fujimura, "Computational fluid dynamic analysis of the initiation of cerebral aneurysms," *Journal of neurosurgery,* vol. 137, no. 2, pp. 335-343, 2021.

[6] M. W. a. P. S. F. Siebert, "Newtonian and non-newtonian blood flow over a backward-facing step–a case study," *Proceedings of the COMSOL Conference, Boston,* vol. 27, 2009.

[7] S. a. S. M. Gholampour, "Effect of bifurcation in the hemodynamic changes and rupture risk of small intracranial aneurysm," *Neurosurgical Review,* vol. 44, no. 3, pp. 1703-1712, 2020.

[8] L. S. M. A. H. M. A. M. U. M. M. S. A. N. H. M. T. a. R. H. Hong, "Modeling and simulation of blood flow analysis on simplified aneurysm models," *IOP Publishing,* vol. 917, no. 1, p. 012067, 2020.

[9] A. M. N. R. D. a. E. M. T.-e. Hussain, "Mathematical analysis of unsteady blood flow through bifurcated abdominal aorta featured aneurysm," *Alexandria Engineering Journal,* vol. 75, pp. 589-604, 2023.

[10] I. F. L. C. L. a. J. S. Husain, " A comparison of Newtonian and non-Newtonian models for pulsatile blood flow simulations," *Journal of the Mechanical Behaviour of Materials,* vol. 21, no. 5-6, pp. 147-153, 2013.

[11] J. H. D. T. T. Y. S. W. J. H. G. E. L. K. a. J. K. S. T. Lim, "The interdependent hemodynamic influence between abdominal aortic aneurysm and renal artery stenosis," *Scientific Reports,* vol. 14, no. 1, p. 31986, 2024.

[12] R. S. G. a. A. C. Singla, "A computational fluid dynamics-based model for assessing rupture risk in cerebral arteries with varying aneurysm sizes," *Mathematical and Computational Applications,* vol. 28, no. 4, p. 90, 2023.

[13] M. N. Uddin, "Numerical study of blood flow through stenotic and aneurysmatic artery of human organ," 2018.

[14] A. G. K. Y. a. T. A. Rahma, "Blood flow CFD simulation on a cerebral artery of a stroke patient," *SN Applied Sciences,* vol. 4, no. 10, p. 261, 2022.

[15] M. J. M. Z. I. B. a. M. F. Uddin, "Numerical computation of pulsatile hemodynamics and diagnostic concern of coronary bifurcated artery flow for Newtonian and non-Newtonian fluid," *Heliyon,* vol. 9, no. 7, 2023.

[16] H. L. L. J. A. H. L. I. Y. S. D. Z. K. S. W. e. a. Liu, "Comparison of Newtonian and non-Newtonian fluid models in blood flow simulation in patients with intracranial arterial stenosis," *Frontiers in physiology,* vol. 12, p. 718540, 2021.

[17] M. S. S. A. C. V. T. S. F. C. S. L. R. &. R. J. Souza, "Fluid flow and structural numerical analysis of a cerebral aneurysm model," *Fluids,* vol. 7, no. 3, p. 100, 2022.

[18] K. Y. K. N. K. a. C. V. I. Tzirakis, "Classification of blood rheological models through an idealized symmetrical bifurcation," *Symmetry ,* vol. 15, no. 3, p. 630, 2023.

[19] C. &. K.Atalik, "Effects of blood viscoelasticity on pulsatile hemodynamics in arterial aneurysms," *Journal of Non-Newtonian Fluid Mechanics,* vol. 279, p. 104263, 2020.

[20] H. &. C.Podder, "Hemodynamical behavior analysis of anemic, diabetic, and healthy blood flow in the carotid artery," *Heliyon,* vol. 10, no. 4, p. e26622, 2024.

[21] H. H. A. M. H. M. A. H. T. D. &. R. S. Afrouzi, "Simulation of blood flow in arteries with aneurysm: Lattice Boltzmann Approach (LBM)," *Computer methods and programs in biomedicine,* vol. 187, p. 105312, 2020.

[22] A. A. G. a. A. E. Elhanafy, "Numerical simulation of blood flow in abdominal aortic aneurysms: Effects of blood shear-thinning and viscoelastic properties," *Mathematics and Computers in Simulation,* vol. 160, pp. 55-71, 2019.

[23] A. M. N. R. D. a. E. M. T.-E. Hussain, "Effects of stenosis and aneurysm on blood flow in stenotic-aneurysmal artery," *Heliyon,* vol. 9, no. 7, 2023.

[24] K. Y. K. N. K. a. C. V. I. Tzirakis, "The effect of blood rheology and inlet boundary conditions on realistic abdominal aortic aneurysms under pulsatile flow conditions," Bioengineering, vol. 10, no. 2, p. 272, 2023.

[25] B. J. N. R. A. S. C. V. N. M. K. S. K. .. &. P. B. P. Sudhir, "Computational fluid dynamics: Simulation studies in cerebral aneurysms," *OPINIONS IN Medical Sciences, Technology and Health,* vol. 1, no. 3, pp. e23021-e23021, 2023.